Dalton Transactions

Accepted Manuscript

ROYAL SOCIETY OF CHEMISTRY

www.rsc.org/dalton

Lanthano phosphomolybdate-decorated silica nanoparticles: novel hybrid materials with photochromic properties

Tânia V. Pinto,[a] Diana M. Fernandes,[a] Clara Pereira,[a,*] Alexandra Guedes,[b] Ginesa Blanco,[c] Jose M. Pintado,[c] Manuel F. R. Pereira[d] and Cristina Freire[a,*]

[a] REQUIMTE, Departamento de Química e Bioquímica, Faculdade de Ciências, Universidade do Porto, 4169-007 Porto, Portugal

[b] Centro de Geologia e Departamento de Geociências, Ambiente e Ordenamento do Território, Faculdade de Ciências, Universidade do Porto, 4169-007 Porto, Portugal

[c] Departamento de Ciencia de Materiales e Ingeniería Metalúrgica y Química Inorgánica, Facultad de Ciencias, Universidad de Cádiz, Campus Rio San Pedro, 11510 Puerto Real, Cádiz, Spain

[d] Laboratório de Catálise e Materiais (LCM), Laboratório Associado LSRE/LCM, Departamento de Engenharia Química, Faculdade de Engenharia, Universidade do Porto, 4200-465 Porto, Portugal

*** Corresponding authors:** Dr. Cristina Freire: Tel: +351 220402590. Fax: +351 220402659. E-mail: acfreire@fc.up.pt. Dr. Clara Pereira: Tel: +351 220402576. Fax: +351 220402659. E-mail: clara.pereira@fc.up.pt

Keywords: Silica nanoparticles, Lanthano phosphomolybdates, Keggin-type phosphomolybdate, Photochromism, Hybrid materials

Abstract

Novel photochromic hybrid nanomaterials were prepared through the immobilization of the lacunary Keggin-type phosphomolybdate ($TBA_4H_3[PMo_{11}O_{39}]\cdot xH_2O$, denoted as PMo_{11}) and sandwich-type lanthano phosphomolybdates ($K_{11}[Ln^{III}(PMo_{11}O_{39})_2]\cdot xH_2O$, denoted as $Ln(PMo_{11})_2$, where Ln^{III} = Sm, Eu, Gd, Tb and Dy) onto positively-charged functionalized silica nanoparticles. The functionalized silica nanoparticles were prepared by a one-step co-condensation route between tetraethylorthosilicate and dimethyloctadecyl[3-(trimethoxysilyl)propyl]ammonium chloride, presenting an average particle size of 95 ± 26 nm, spherical morphology and pore diameter of 13.7 nm. All characterization techniques proved the successful immobilization of the phosphomolybdates. The photochromic properties of the resulting hybrid nanomaterials in the solid state were evaluated by UV-Vis spectroscopy and colorimetry. All materials revealed promising photochromic properties under UV irradiation (λ = 254 nm). The lacunary phosphomolybdate anchored onto the silica nanoparticles, C18-SiO_2@PMo_{11}, showed the best photoswitching properties, with the color changing from green to dark-blue (ΔE^* = 26.8). Among the $Ln(PMo_{11})_2$-based hybrid nanomaterials, those containing higher Mo loadings – Eu^{III}- and Tb^{III}-based samples – presented more significant color changes from green to dark-blue (ΔE^* = 18.8–18.9). These results revealed that the optical properties of the as-prepared hybrid nanomaterials did not depend directly on the type of Ln^{III} cation, but only on the amount of Mo, which was the target element responsible for the photochromic behavior.

Introduction

Photochromic materials have attracted much attention in several fields, due to their optical properties change in response to light. They have remarkable potentialities for important commercial applications, including sunlight-responsive eyewear, protection (in spectacles, photo-barriers, anti-counterfeiting, and camouflage), cosmetics, decoration, textiles, optical data storage, optical switching devices, solar energy storage, biological systems, and so on.[1–3] Even though so far most photochromic compounds are organic because of their good performance in a broad wavelength range,[4] inorganic materials present some advantages over the organic counterparts: they have better thermal and chemical stability, mechanical strength, and shape molding (can be easily shaped as thin films, coatings, monoliths, etc.).[4,5] Among inorganic materials, polyoxometalates (POMs), a unique class of inorganic metal-oxygen cluster anions, are promising candidates for photochromic applications due to their structural, chemical, and redox properties.[6–9] Purely inorganic POMs are not photochromic but can be easily converted into mixed-valence colored species ("heteropolyblues" or "heteropolybrowns") when conjugated with organic proton donor counter-cations due to the POM ability to reversibly exchange a large number of electrons without decomposing or suffering changes on its structural arrangement.[6,9] To date, most of the characterized photochromic POM materials are primary, secondary or tertiary alkylammonium salts of polyoxomolibdates.[10] Yamase *et al.* discussed the photochromic mechanism underlying this type of hybrid systems in terms of intermolecular hydrogen donation involving the counter-cation and intramolecular electron transfer, with photo-reduction of Mo^{VI} species to Mo^{V} under UV irradiation.[6,10,11] More recent studies revealed that the photogenerated colors of these organic-inorganic hybrids are intrinsically dependent on the composition and the

topology of the POMs, while their coloration and fading kinetics are associated with the nature of the organic counter-cations.[11] Moreover, the properties of these materials are strongly connected with the interface and synergy between both organic and inorganic moieties.[10]

Although POMs represent an outstanding class of molecular building blocks for the construction of functional materials with photochromic properties their practical technological applications are limited due to their poor processability and compatibility with other materials.[12,13] To overcome these problems, some strategies have been developed based on their incorporation in several supports, mostly through non-covalent interactions (electrostatic interactions): immobilization on electrodes, metals and oxide surfaces, encapsulation in polymers, hierarchical self-assembly of surfactant-encapsulated POMs, incorporation in layer-by-layer assemblies using positively-charged polyelectrolytes and in Langmuir-Blodgett films.[14] Regarding oxide surfaces, silica supports are of special interest since they possess a variety of important features, such as large surface area, tunable surface properties and high chemical and mechanical stability.[15,16] In this context, mesoporous bulk silicas have been used as supports for the immobilization of photochromic POMs by co-condensation and direct post-grafting, both based on covalent bonding and by impregnation.[17] Photochromic POMs have also been introduced in bulk silica matrices by sol-gel to produce POM/silica hybrid films.[18]

With the advances in Nanotechnology, nanometer-sized silica supports emerged as potential alternatives to their bulk counterparts, due to their large surface area to volume ratio which enables the incorporation of a higher loading of functional groups, high colloidal stability in several solvents and biocompatibility.[15,16]

However, to the best of our knowledge, only photoluminescent Ln^{III}POMs have been incorporated onto silica nanoparticles (SNPs) and no work concerning the

immobilization of photochromic POMs on SNPs has been reported. The photoluminescent silica nanocomposites and core-shell silica nanoparticles have been prepared through the incorporation of Ln^{III} complexes bearing 3-hydroxypicolinate ligands or polyoxotungstate-based anions (Keggin-type) in silica nanoparticles by sol-gel method and reverse microemulsion.[19–23] Furthermore, the reported Ln^{III}POM immobilization procedures often require the use of additional steps for surfactant removal, non-aqueous solvents or lead to low nanomaterial yields, which limits their scalability for industrial applications. In this context, the development of new processes for the production of photoresponsive hybrid POM-based SNPs in high yields with photochromic properties is highly desired.

In this work we report the preparation of novel photochromic hybrid nanomaterials through the non-covalent immobilization of the lacunary Keggin-type phosphomolybdate ($TBA_4H_3[PMo_{11}O_{39}]\cdot xH_2O$), and sandwich-type lanthano phosphomolybdates with general formula $K_{11}[Ln^{III}(PMo_{11}O_{39})_2]\cdot xH_2O$, where Ln^{III} = Sm, Eu, Gd, Tb and Dy, onto positively-charged SNPs. A new strategy for the scalable design of these photochromic hybrid SNPs is proposed based on electrostatic interactions. The POMs post-grafting onto the positively-charged SNPs proposed herein, instead of the conventional POM encapsulation approach, constitutes a potential route to improve the control of the amount of anchored POM while preserving the intrinsic morphological and textural features of the SNPs. Additionally and to the best of our knowledge, a systematic study concerning the influence of the type of Ln^{III} cation on the morphological, textural, chemical and photochromic properties of the resulting POM-based hybrid SNPs is for the first time reported. The hybrid silica nanomaterials were prepared by a two-step procedure involving: (1) the synthesis of positively-charged SNPs by aqueous co-condensation between tetraethyl orthosilicate and

tetraalkylammonium organosilane under mild alkaline conditions, followed by the (2) post-immobilization of $TBA_4H_3[PMo_{11}O_{39}]\cdot xH_2O$ or $Ln^{III}POM$ onto the SNPs. The nanomaterials were characterized in terms of morphology, particle size, textural properties and chemical composition. The photochromic properties in the solid state were evaluated by UV-Vis spectroscopy and colorimetry before and after UV-irradiation (λ = 254 nm). The influence of the type of phosphomolybdate and Ln^{III} cation (in the case of the sandwich-type lanthano phosphomolybdates) on the degree of functionalization, morphological, textural and photochromic properties of the resulting hybrid materials was investigated.

Experimental section

Materials, reagents and solvents

All reagents and solvents were used as received without further purification. Tetraethyl orthosilicate (TEOS, ≥99%) was purchased from Fluka, triethanolamine (TEA, ≥99%) and dimethyloctadecyl[3-(trimethoxysilyl)propyl]ammonium chloride solution (C18, 42 wt% in methanol) were supplied by Sigma-Aldrich. Ethanol and acetonitrile (analytical grade) were purchased from Merck and Fisher Chemical, respectively. Ultrapure water (Millipore, specific resistivity: 18 MΩ cm) was used throughout the experiments.

The tetrabutylammonium ($C_{16}H_{36}N$, TBA) and potassium salts of the lacunary phosphomolybdate ($TBA_4H_3[PMo_{11}O_{39}].xH_2O$) and sandwich-type lanthano phosphomolybdates ($K_{11}[Ln(PMo_{11}O_{39})_2].xH_2O$ with Ln^{III} = Sm, Eu, Gd, Tb and Dy) used in the preparation of the photochromic hybrid materials were synthesized following procedures described in literature.[8,24] For simplification, the lacunary and lanthano phosphomolybdates will be denoted as PMo_{11} and $Ln(PMo_{11})_2$, respectively.

Preparation of C18-functionalized SNPs

The positively-charged C18-functionalized SNPs were synthesized by co-condensation between TEOS and C18 organosilane, using TEA as base, following a procedure adapted from literature.[25–27]

A stock solution containing 64.0 cm^3 of water (3.55 mol) and 10.5 cm^3 of methanol (0.259 mol) was stirred for 10 min at room temperature. To this solution, 4.1 cm^3 of TEA (0.031 mol) were added, resulting in a pH of approximately 11. Subsequently, 60.0 cm^3 of this solution were heated to 60 °C in an oil bath, and then 4.35 cm^3 of TEOS (19.5 mmol) and 8.70 cm^3 of C18 (6.5 mmol) were simultaneously added dropwise under vigorous stirring. The reaction mixture was stirred at 60 °C for 2 h and then cooled to room temperature. After that, 150 cm^3 of methanol were added and the resulting material, C18-SiO_2, was isolated by centrifugation at 16000 rpm during 20 min. Afterwards the C18-SiO_2 nanomaterial was washed/centrifuged with ethanol twice, and finally dried at 100 ºC overnight under vacuum.

Preparation of the photochromic hybrid nanomaterials

The photochromic hybrid nanomaterials were prepared by immobilization of PMo_{11} or $Ln(PMo_{11})_2$ onto C18-SiO_2. A solution of 150 mg of PMo_{11} or $Ln(PMo_{11})_2$ in 80 cm^3 of acetonitrile or water, respectively, was added to 500 mg of C18-SiO_2. The resulting mixture was refluxed for 24 h with vigorous stirring and the final material was isolated by centrifugation (16000 rpm during 20 min). In order to remove physically adsorbed PMo_{11} or $Ln(PMo_{11})_2$, the resulting nanomaterials were refluxed in 80 cm^3 of ethanol or water, respectively, during 1 h and then centrifuged at 16000 rpm for 20 min. This last step was repeated once with ethanol (80 cm^3). All hybrid nanomaterials were

dried under vacuum at 100 ºC overnight. The resulting nanomaterials will be denoted as C18-SiO_2@PMo_{11} and C18-SiO_2@$Ln(PMo_{11})_2$, where Ln^{III} = Sm, Eu, Gd, Tb and Dy.

Physicochemical characterization

Fourier transform infrared spectroscopy-attenuated total reflectance (FTIR-ATR) spectra were obtained on a Perkin-Elmer Spectrum 100 spectrophotometer equipped with an ATR accessory in the range of 4000–650 cm^{-1}, with 4 cm^{-1} resolution and 16 scans.

Raman spectra were recorded at room temperature on a Jobin-Yvon LabRaman spectrometer equipped with a CCD camera using a He-Ne laser at an excitation wavelength of 632.8 nm and a power of 20 mW. An Olympus BX40 optical microscope with a 50× objective lens was used to focus the laser beam on the sample and collect the scattered radiation. In order to prevent fluorescence, all spectra were acquired in the range of 1800–400 cm^{-1}, with 20 scans during 10 seconds.

Molybdenum contents obtained by inductively coupled plasma atomic emission spectrometry (ICP-AES) and nitrogen, carbon and silicon elemental analyses (EA) were performed at Laboratório de Análises do Instituto Superior Técnico (Lisboa, Portugal).

The X-ray photoelectron spectroscopy (XPS) was performed in a Kratos Axis Ultra DLD spectrometer equipped with a monochromatic Al Kα radiation (1486.6 eV), with the X-ray source being operated at 150 W. In order to determine the initial oxidation state of the Mo species, prior to the XPS characterization using the 150 W power source, an X-ray source with lower power (50 W) and a lower data acquisition time were used. The powdered samples were pressed into pellets prior to the XPS studies. To correct possible deviations caused by the electric charge of the samples, the calibration of the binding energies was performed by using the C 1s band at 284.6 eV

(C–H/C–C) as internal reference. The XPS spectra were deconvoluted with CasaXPS software, using non-linear least squares fitting routine after a Shirley-type background subtraction. The surface atomic percentages were calculated from the corresponding peak areas and by using the sensitivity factors provided by the manufacturer.

Scanning electron microscopy (SEM) and energy-dispersive X-ray spectroscopy (EDS) were performed at Centro de Materiais da Universidade do Porto (CEMUP, Porto, Portugal), using a high-resolution environmental scanning electron microscope (FEI Quanta 400 FEG ESEM) equipped with an energy-dispersive X-ray spectrometer (EDAX Genesis X4M). All samples were analyzed as powders both uncoated and coated with a thin gold-palladium film.

Nitrogen adsorption-desorption isotherms at –196 °C were measured in an automatic Quantachrome NOVA Surface Area and Pore Size analyzer apparatus. All samples were degassed at 120 ºC under vacuum for 3 h. Surface area calculations were performed using the Brunauer–Emmett–Teller (BET) equation in the range of $P/P_0 < 0.3$. The pore diameter and pore volume were determined using the BJH method from the desorption branch.[28]

In order to evaluate the photochromic properties of the hybrid materials, the samples were irradiated with an Eversun UVA fluorescent lamp (OSRAM, L40W/79K) which mainly emitted in the wavelength range of 310–390 nm (with maximum intensity at 355 nm). The irradiation time and the distance between the sample and the lamp were 17 h and 15 cm, respectively. The spectral reflectance and CIELab values of the samples were acquired on a reflectance spectrophotometer Datacolor Spectraflash SF 450 in the range of 400–700 nm. The spectrophotometer was programmed with the following settings: circular measurement area of 9 mm of diameter with a specular component included; CIE Standard Illuminant D65 corresponding to average daylight at

a temperature of 6230 ºC, including the ultraviolet wavelength region; CIE 1964 Standard Observer (10° Observer). The spectrophotometer was set to perform three sequential measurements, giving the color coordinates average. The calibration of the spectrophotometer was performed with white and black reference standards according to the manufacturer instructions. The CIELAB system provides a psychometric lightness index L*, which is a chromatic measure in a scale ranging from 0 (black) to 100 (white), and two color coordinates a*, a green-red continuum (positive values for reddish colors and negative values for greenish ones), and b*, a blue-yellow continuum (positive values for yellowish colors and negative for the bluish ones). The total color difference (ΔE*) between UV irradiated and non-UV irradiated hybrid nanomaterials was calculated from L*, a* and b* values, using the following equation: $\Delta E^* = ((\Delta L^*)^2 + (\Delta a^*)^2 + (\Delta b^*)^2)^{½}$, where $\Delta L^* = L^*_{\text{UV irradiated}} - L^*_{\text{non-UV irradiated}}$; $\Delta a^* = a^*_{\text{UV irradiated}} - a^*_{\text{non-UV irradiated}}$; $\Delta b^* = b^*_{\text{UV irradiated}} - b^*_{\text{non-UV irradiated}}$.

Results and discussion

Structural and chemical properties

All materials were characterized by FTIR-ATR and Raman spectroscopy to confirm the one-pot functionalization of the SNPs with C18 by co-condensation and the phosphomolybdates immobilization procedures, through the identification of the characteristic vibrational modes of the organic and inorganic moieties. The FTIR-ATR spectrum of C18-SiO_2 (Fig. 1) exhibits the typical bands of the silica network: Si–O–Si asymmetric stretching (1057 cm^{-1} with a shoulder around 1200 cm^{-1}), Si–O stretching of Si–OH and $Si–O^-$ groups (945 cm^{-1}) and Si–O–Si symmetric stretching (795 cm^{-1}) vibrations.[26,27,29,30] Additionally, the spectrum presents characteristic bands of the C18 organosilane including those related with C–H stretching (2956 and 2853 cm^{-1}), N^+–C

bending (1482 cm^{-1}), C–H bending (1466 cm^{-1}) and CH_2 rocking (720 cm^{-1}) vibrational modes, confirming the successful functionalization of the SNPs with C18.[26,27,29–31] The FTIR-ATR spectra of the free phosphomolybdate-based compounds (illustrated in Fig. S1 in the Supplementary Information) display the typical vibrational modes of the Keggin framework in the wavenumber region of 1100–800 cm^{-1} such as P–O_a asymmetric stretching (1080 and 1031 cm^{-1}), Mo–O_d asymmetric stretching (925 cm^{-1}), Mo–O_b–Mo asymmetric stretching (864 cm^{-1}) and Mo–O_c–Mo asymmetric stretching (806 cm^{-1}), where O_a is the oxygen of the central tetrahedron, O_b is the bridging oxygen coordinated to two Mo atoms through corner-shared Mo octahedra, O_c is the bridging oxygen coordinated to two Mo atoms through edge-shared Mo octahedra, and O_d is the terminal oxygen.[8,24,32–34] Upon the immobilization of PMo_{11} or $Ln(PMo_{11})_2$ onto the C18-SiO_2 nanoparticles (illustrated in Fig. 1 for C18-SiO_2@$Tb(PMo_{11})_2$ and in Fig. S2 in the Supplementary Information for the remaining hybrid nanomaterials) it is possible to detect two bands around 900 and 863 cm^{-1}, which can be attributed to the Mo–O_d and Mo–O_b–Mo asymmetric stretching vibrational modes,[35] respectively, confirming the immobilization of the phosphomolybdates onto the nanosilica matrix and the preservation of their structure. Moreover, for all hybrid nanomaterials a slight red-shift of these two bands can be observed when compared with the spectra of the free POMs, which, according to literature, can be related not only to the strong electrostatic interactions between the negatively charged heteropolyanions and the positively charged quaternary ammonium organosilane (N^+–C), but also to the partial formation of "heteropolyblue" species by reduction of some Mo^{VI} species to Mo^{V} during the immobilization procedure.[36–40] The FTIR-ATR bands associated with P–O_a and Mo–O_c–Mo asymmetric stretching vibration modes (1080, 1031 and 806 cm^{-1}, respectively) cannot be detected since they are overlapped by the strong intensity bands associated

with Si–O–Si asymmetric and symmetric stretching vibrations, respectively. Similar results were obtained for all hybrid materials (Fig. S2 in the Supplementary Information).

Fig. 1

Raman spectroscopy was used to provide additional information concerning the immobilization of the phosphomolybdates onto the C18-SiO_2 nanoparticles. The Raman spectra of the lacunary PMo_{11} and $Ln(PMo_{11})_2$ compounds (Fig. S3 in the Supplementary Information) show the characteristic bands of the Keggin framework in the low wavenumber region 1100–400 cm^{-1}, such as those associated with Mo=O_d symmetric stretching (973 cm^{-1}), Mo–O_b–Mo asymmetric stretching (863 cm^{-1}) and Mo–O_c–Mo symmetric stretching (~620 cm^{-1}) vibrations.[24,32] The shoulder around 964 cm^{-1} and the band at 946–932 cm^{-1} can be attributed to Mo=O_d asymmetric stretching vibrations modes.[24,32] In the Raman spectra of all hybrid materials (illustrated in Fig. 2 for C18-SiO_2@Tb$(PMo_{11})_2$ and in Fig. S4 in the Supplementary Information for the other hybrid nanomaterials), the most intense bands of the phosphomolybdates located at 973 and 951 cm^{-1} (assigned to the Mo-O_d symmetric and asymmetric stretching vibrational modes, respectively) can be detected, proving their successful immobilization onto the C18-SiO_2 nanoparticles, in accordance with FTIR-ATR results. The remaining bands (from Mo–O_b–Mo asymmetric stretching vibrations and Mo–O_c–Mo symmetric stretching vibrations) are not clearly visible because the characteristic vibrational modes of the C18-SiO_2 structure occur in the same region (Fig. 2A).

Fig. 2

The chemical composition of C18-SiO_2 before and after the phosphomolybdates immobilization was quantified by chemical analysis and XPS. The chemical analysis (Table 1) of C18-SiO_2 reveals the presence of 32.8 and 1.4 mmol g^{-1} of carbon and nitrogen, respectively, confirming the successful silica functionalization with the C18 organosilane. A higher amount of carbon and an almost similar amount of nitrogen were detected by XPS (surface contents of 45.6 and 1.2 mmol g^{-1}, respectively), which leads to the conclusion that the C18 organosilane is preferentially located on the surface of the SiO_2 nanomaterial. Furthermore, the carbon/nitrogen molar ratio obtained by EA (23.4) is in accordance with that predicted theoretically taking into account the amount of C18 organosilane used during the co-condensation reaction (~23–24, assuming the C18 covalent grafting through 3 or 2 methoxy groups), which indicates that the structure of the organosilane was preserved upon its incorporation on the silica framework.

Table 1

Upon immobilization of the phosphomolybdates, the bulk contents of silicon, carbon and nitrogen elements obtained by chemical analysis do not change significantly and molybdenum is detected in all hybrid nanomaterials (Table 1), which demonstrates the successful incorporation of the POMs onto the C18-modified SNPs. Moreover and as expected, the C18-SiO_2@Ln$(PMo_{11})_2$-based nanomaterials present higher amount of molybdenum than C18-SiO_2@PMo_{11} since the sandwich-type lanthano phosphomolybdates are composed by two lacunary PMo_{11} units.[8,24,32,41] The Eu and Tb-based hybrid nanomaterials are those which contain the highest Mo loadings. Concerning the immobilization efficiency, the Mo contents obtained by ICP-AES are

close to the values predicted theoretically (1.6–1.8 mmol g^{-1}) taking into account the amount of $Ln(PMo_{11})_2$ added during the immobilization procedure and assuming that the immobilization occurs through electrostatic interactions, being close to 100% for Eu- and Tb-based hybrid nanomaterials. Identical results were obtained by XPS analysis, revealing that the Eu- and Tb-based hybrid nanomaterials are those with higher Mo 3d surface content (1.9 and 1.6 mmol g^{-1}, respectively). Furthermore, the Mo surface contents determined by XPS analysis are of the same order of magnitude as those obtained by ICP-AES (0.5–1.9 mmol g^{-1} *vs.* 0.8–1.7 mmol g^{-1}, respectively), which indicates that the POM units are homogeneously distributed throughout the C18-SiO_2 framework.

The XPS analysis provided information about the surface atomic percentages (At%) of all elements on the nanomaterials surface (Table 2), besides those quantified by chemical analysis, and their core-level binding energies (Table S1 in the Supplementary Information). According to XPS analysis, the C18-SiO_2 sample is mainly composed by oxygen, silicon and carbon and a small quantity of nitrogen, in accordance with the results from chemical analysis (Table 2). The O 1s and Si 2p high-resolution spectra of C18-SiO_2 (Fig. S5 and Table S1 in the Supplementary Information) exhibit bands centered at 532.2 and 102.7 eV (for the Si $2p_{3/2}$ component), respectively, which are typical values for lattice oxygen and silicon in pure silica.[26] In both O 1s and Si 2p spectra are also observed bands at 533.8 and 104.0 eV (for the second Si $2p_{3/2}$ component), respectively, which are related to O–C and Si–C bonds from the organosilane.[26] The high-resolution C 1s spectrum (Fig. S5 and Table S1 in the Supplementary Information) can be deconvoluted into four components, with the main ones, centered at 284.6, 285.7 and 286.8 eV, being attributed to C–H/C–C, C–N^+ and C–O bonds, respectively, from the organosilane.[26,42,43] The N 1s high-resolution

spectrum (Fig. S5 and Table S1 in the Supplementary Information) presents two bands: the main one at 402.1 eV can be attributed to quaternary ammonium N^+–R_4, while the weak band at 399.3 eV can be assigned to N–H bonds.[42,43]

Table 2

Upon POM immobilization, P, Mo and Ln (Ln = Sm, Eu, Gd, Tb and Dy) elements are also detected (Table 2) confirming the success of the POM anchorage onto the functionalized SNPs. For all the hybrid nanomaterials, the binding energies of the bands in the Si 2p and C 1s high-resolution spectra do not change significantly when compared to those of the parent C18-SiO_2 (Tables S1 and S2 in the Supplementary Information). However, in the case of the O 1s spectra (illustrated in Fig. for C18-SiO_2@Tb(PMo_{11})$_2$) two extra bands can be detected: one at 529.9–530.2 eV, which can be assigned to O–Mo bonds from the anchored POMs[44,45] and a very weak band at 534.7–536.1 eV probably associated with physisorbed water and/or crystallization water molecules from the POM (Tables S1 and S2 in the Supplementary Information).[46] The band associated with the O–P bond cannot be detected since it occurs at a binding energy of 532.2 eV for this family of POMs, being overlapped with the strong intensity band of the O–Si bonds from the silica matrix.[26,44,45] In the case of the N 1s bands, they are partially overlapped with those of Mo 3p (illustrated in Fig. 3 for C18-SiO_2@Tb(PMo_{11})$_2$) which appear in the same binding energy range (Mo $3p_{3/2}$ component bands in the range of 390–404 eV).[44,47] Therefore, in order to determine the surface At% and binding energies of N 1s, the high-resolution XPS spectra occurring in this particular range were deconvoluted into five components: two sets of Mo 3p bands ($3p_{3/2}$ and $3p_{1/2}$) related with Mo^{VI} and Mo^{V} cations, and one band of N 1s. The band

associated with N 1s, at 402.0–402.3 eV, can be attributed to the N^{+}–R_4 bonds from the organosilane.

Fig. 3

In the case of the Mo 3d high-resolution spectra, in previous works it was observed that the exposition of PMo-based samples to the X-ray source during XPS analysis induces the photoreduction of the POMs,[45,48] which increases the concentration of Mo^{V} species relative to those of Mo^{IV}. To overcome this problem, an X-ray source with lower power (50 W) was initially used, as well as lower data acquisition time, in order to determine the initial oxidation state of the Mo species. For all PMo-based samples, the initial oxidation state of Mo species was mainly +6, with a small amount of Mo^{V} cations (At% below 6%). Afterwards, a new measurement was performed, at higher power (150 W) and with higher data acquisition time, to quantify all elements. Comparing the results of these two measurements, as expected, it was observed an increase of the amount of Mo^{V} species for all samples. Although the relative Mo^{V} and Mo^{VI} At% changed, no significant variation was observed regarding their binding energies. In this context, the Mo 3d high-resolution spectra (illustrated in Fig. 3 for C18-SiO_2@Tb(PMo_{11})$_2$), recorded at 150 W, was resolved into two sets of Mo 3d doublets (Mo $3d_{5/2}$ and Mo $3d_{3/2}$) caused by the spin-orbit coupling, with binding energies of 230.8–232.3 and 233.9–235.5 eV, and 231.9–234.2 and 235.1–237.3 eV, respectively (Tables S1 and S2 in the Supplementary Information). The first set is assigned to Mo^{V} cations, whereas the second set is assigned to Mo^{VI}.[48,49]

The Ln surface At% was estimated by deconvolution of the Ln 3d or 4d high-resolution spectra. In the case of Sm- and Gd-based nanomaterials, the Ln At% was

determined by curve fitting of the corresponding Ln 3d high-resolution spectrum since the Ln 4d bands are overlapped with those of P 2p. In the case of C18-SiO_2@Eu(PMo_{11})$_2$ and C18-SiO_2@Tb(PMo_{11})$_2$ hybrids, the Ln 4d high-resolution spectra were used to estimate the Eu and Tb surface contents, despite the Ln bands appearing in the same binding energy range as those of P 2p and Si 2s, respectively. In the case of C18-SiO_2@Tb(PMo_{11})$_2$, the Tb At% could not be calculated using the 3d core-level since the relative sensitivity factor (RSF) of Tb 3d for monochromatic Al Kα radiation (1486.6 eV) is not reported in the literature or XPS libraries. Moreover, the amount of Dy in C18-SiO_2@Dy(PMo_{11})$_2$ could not be estimated since the RSF of Dy 3d is not reported in the literature or XPS libraries and the Dy 4d bands are overlapped with the strong band related with Si 2s.

It should be remarked that the surface amount of Ln^{III} cannot be determined with very high precision by XPS, not only because the low content of Ln within the samples causes a high noise signal in the spectral region, hindering the deconvolution, but also because of the lack of published RSF for Ln 4d/3d and/or overlap with bands from other elements. Therefore, XPS analysis was mainly used to confirm the presence of Ln elements and their oxidation state through their binding energies.

The XPS high-resolution spectra of Sm 3d, Eu 3d and Tb 3d can be fitted into two components assigned to $3d_{5/2}$ and $3d_{3/2}$ bands of Ln in the oxidation state +3 (Sm 3d: 1082.7 and 1109.7 eV, respectively; Eu 3d: 1134.2 and 1163.5 eV; and Tb 3d: 1243.2 and 1277.2 eV). These values are consistent with those reported in the literature.[45,46,50–53] The XPS spectrum of Gd 3d shows only one peak at 1188.3 eV, which corresponds to the Gd^{III} $3d_{5/2}$ band; the Gd^{III} $3d_{3/2}$ component is overlapped with the carbon KLL Auger lines at ~1223 eV.[46,50] Similarly, the Dy^{III} 3d high-resolution spectrum displays only one component ($3d_{5/2}$) at 1303.8 eV.[46,52]

Morphological and textural properties

The morphology of the samples was characterized by SEM-EDS. The SEM image of the C18-SiO_2 nanomaterial (Fig. 4A) shows uniform nanosized spheres with average particle size of 95 ± 26 nm. The EDS spectrum also confirms the organo-funcionalization by the presence of carbon and chlorine peaks, in accordance with XPS. Upon the PMo_{11} immobilization (Fig. 4B) onto the C18-SiO_2 surface, no changes in the morphology and particle size are observed and molybdenum and phosphor are detected in the corresponding EDS spectrum. However, in the case of C18-SiO_2@$Tb(PMo_{11})_2$ in some regions (Fig. 4C Z1) it is possible to verify the existence of spherical-shaped particles, while in other regions (Fig. 4C Z2) several clusters with "needle" shape are visualized. According to the EDS analysis, the Z2 region presents larger amounts of Mo, P and Tb elements, whereas the Z1 area is more enriched in the characteristic elements of the functionalized SNPs and Mo. These results suggest that the negatively-charged $[Tb(PMo_{11})_2]^{11-}$ units have a high tendency to form clusters in the C18-SiO_2 surface in order to preserve their integrity and stability as a result of charge differences (POM *vs.* SNPs surface charge). Furthermore, it has been reported that lanthano phosphomolybdates, in the absence of solvent, recrystallize in needle-like shape. This behaviour was confirmed for the remaining C18-SiO_2@$Ln(PMo_{11})_2$-based nanomaterials.

Fig. 4

The N_2 adsorption-desorption isotherms at –196 ºC (Figs. 5 and S6 in the Supplementary Information and Table 3) reveal that all materials present a not well-

defined type of isotherm, although a type IV can be expected since it better describes the adsorption on a material composed by packed nanosized spheres (Fig. 4), with a clear hysteresis typical of materials exhibiting mesoporosity with a very wide pore size distribution.

These observations suggest that the immobilization process does not induce changes in the textural properties of the parent C18-SiO_2. The specific surface area (A_{BET}) values calculated according to the BET theory[28] are relatively small, in the range of 16–33 m^2 g^{-1}, with the corresponding pore volumes (V_p), calculated by the BJH method,[28] being in the range of 0.07–0.17 cm^3 g^{-1}. The slight decrease of the specific surface areas and pore volumes relative to those of the parent C18-SiO_2 are more notable in the case of the $Ln(PMo_{11})_2$-based materials, probably due to the larger dimensions of the anchored lanthano phosphomolybdates.

Fig. 5

Table 3

Photochromic properties

The diffuse reflectance spectra of all the parent phosphomolybdates exhibit two absorption bands in the λ = 200–350 nm region (not shown): the band at λ_{max} = 355 nm is characteristic of the Keggin structure and is attributed to a ligand-to-metal-charge transfer transition (LMCT) from the bridging oxygen atoms O_b and O_c to the Mo^{VI} cations ($O_{b,c} \rightarrow Mo^{VI}$) and the band at λ_{max} = 247 nm is attributed to the LMCT transition from the terminal oxygen atoms to the Mo^{VI} cations ($O_t \rightarrow Mo^{VI}$).[6,37] No absorption bands are observed in the visible region due to the d^0 electronic configuration of the Mo^{VI} species.[6]

The diffuse reflectance spectra of the corresponding POM-based hybrid nanomaterials (Fig. 6a) exhibit a new broad band centered at $\lambda \sim 730$ nm, but no significant changes are observed in the UV bands, which is indicative of the preservation of the POM structure during the immobilization process. This broad absorption band is assigned to the intervalence charge transfer (IVCT) of $Mo^{V} \rightarrow Mo^{VI}$,[35,40] but it may also mask the d-d transition of d^1 Mo^{V} species ($\lambda \sim 530$ nm). The appearance of this band suggests a reduction of some molybdenum cations (Mo^{VI} to Mo^{V}) by electron transference from the organosilane (electron donor) to the heteropolyanion (electron acceptor), leading to the formation of "heteropolyblues". The occurrence of this partial reduction could, possibly, be induced not only by the difficulty of keeping compounds in the dark during synthesis and manipulation, but also by the temperature applied during the immobilization procedure. Although all hybrids show similar spectroscopic behavior, the position of the absorption maximum and its intensity are slightly different. The hybrid nanomaterials show different colorations: PMo_{11}, $Eu(PMo_{11})_2$ and $Tb(PMo_{11})_2$-based nanomaterials present a yellow-green color, while the other hybrids ($Sm(PMo_{11})_2$, $Gd(PMo_{11})_2$ and $Dy(PMo_{11})_2$-based materials) exhibit a paler yellow color.

Fig. 6

After UV irradiation (Fig. 6b), the intensity of the broad band increases, with the λ_{max} shifting to lower wavenumbers, which indicates an increase of the amount of reduced molybdenum species.[35,40] Simultaneously, the coloration of all hybrid nanomaterials also changes: from yellow-green to blue (PMo_{11}, $Eu(PMo_{11})_2$ and

$Tb(PMo_{11})_2$) and from pale-yellow to yellow-green ($Sm(PMo_{11})_2$, $Gd(PMo_{11})_2$ and $Dy(PMo_{11})$).

After removal of the UV light source, the bleaching process takes place gradually in air. However, if the UV-irradiated materials are stored in nitrogen, helium, argon or vacuum conditions, their color would remain for a long time. When changing the ambient atmosphere to air or oxygen, the bleaching process takes place[40] and can be accelerated under moderate heating conditions (~80ºC).[17]

Although all hybrid nanomaterials present photochromic response under UV irradiation, they do not exhibit the same colorimetric characteristics. CIELAB color values (L*, a*, b*) and color difference ΔE* between UV irradiated and non-UV irradiated silica-based hybrid nanomaterials are presented in Table 4. In the b* *vs.* a* plot (Fig. **7**) it can be observed that before UV irradiation the color of all samples is situated in the negative and positive areas of the a* and b* coordinates, respectively (namely, in the green-yellow quadrant). The PMo_{11}, $Eu(PMo_{11})_2$ and $Tb(PMo_{11})_2$-based hybrid materials have lower values of L*, presenting more negative a* values and more positive b* values, which means that the yellow-green component is higher in this group. In the case of $Sm(PMo_{11})_2$, $Gd(PMo_{11})_2$ and $Dy(PMo_{11})_2$-based nanomaterials, they have higher L* values, with higher a* values and lower b* values and, as a result, they present a paler yellow color. After UV irradiation (Fig. 8), all samples change their color and become darker ($\Delta L^* < 0$). For the PMo_{11}, $Eu(PMo_{11})_2$ and $Tb(PMo_{11})_2$-based nanomaterials significant changes are observed as their color shifts to the green-blue quadrant: their color changes from green to blue (negative values of b*, while the values of a* barely change). On the other hand, the $Sm(PMo_{11})_2$, $Gd(PMo_{11})_2$ and $Dy(PMo_{11})_2$ group remains in the same quadrant but their color become less pale and more yellow-green (more negative a* and more positive b*).

As expected, the C18-SiO_2@PMo_{11} shows the highest photochromic response ($\Delta E^* = 26.9$) due to the higher tendency of PMo_{11} to be reduced. Among the $Ln(PMo_{11})_2$-based nanomaterials, the europium and terbium-based samples show the highest ΔE^*, implying that their color changes are more perceptible, which is in accordance with their higher Mo loading (1.7 mmol g^{-1}) among the series. In a previous study[8] it was found that the presence of different Ln^{III} ions had no effect on the Mo-based redox processes. Therefore, these results are directly influenced by the amount of Mo on the nanosilica matrix.

Fig. 7

Fig. 8

Table 4

Conclusions

The lacunary Keggin-type phosphomolybdate (PMo_{11}) and sandwich-type lanthano phosphomolybdates ($Ln(PMo_{11})_2$, where Ln^{III} = Sm, Eu, Gd, Tb and Dy) were successful incorporated onto positively-charged functionalized SNPs. The functionalized SNPs showed an average particle size of 95 ± 26 nm, spherical morphology and pore diameter of 13.7 nm. The FTIR-ATR and Raman spectroscopy techniques proved the immobilization of the phosphomolybdates onto the nanosilica matrix and the preservation of their structure. Furthermore, the occurrence of a slight red-shift of the FTIR-ATR bands assigned to Mo–O_d and Mo–O_b–Mo asymmetric stretching vibrational modes could be related not only to the strong electrostatic interactions between the negatively charged heteropolyanions and the positively charged quaternary ammonium organosilane (N^+–C), but also to the "partial" formation

of "heteropolyblue" species by reduction of some Mo^{VI} to Mo^{V} cations during the immobilization procedure. The Mo contents obtained by ICP-AES were close to those predicted theoretically, being close to 100% for Eu- and Tb-based hybrid nanomaterials. In addition, the Mo surface contents determined by XPS were of the same order of magnitude as those obtained by ICP-AES, which showed that the POM units were homogeneously distributed through the C18-SiO_2 framework. The XPS also proved the mixed oxidation state of Mo (Mo^{V} and Mo^{VI}) and the presence of the lanthanides. All materials revealed promising photochromic properties under UV irradiation (λ = 254 nm): the C18-SiO_2@PMo_{11} showed the best photoswitching properties due to the higher tendency of PMo_{11} to be reduced, with the color changing from green to dark-blue (ΔE^* = 26.8). Among the $Ln(PMo_{11})_2$-based hybrid nanomaterials, those of Eu^{III} and Tb^{III} were the most promising due to their higher Mo loading, with the color also changing from green to dark-blue (ΔE^* = 18.8–18.9), in accordance with the C18-SiO_2@PMo_{11} nanomaterial. Finally, the optical properties of the $Ln(PMo_{11})_2$-based hybrid nanomaterials did not depend on the type of Ln^{III} cation, but only on the Mo loading, revealing that the lanthanide cation did not affect directly the Mo-based redox processes, which are responsible for the photochromic behavior.

Acknowledgments

This work was funded by Fundação para a Ciência e a Tecnologia (FCT) and FEDER through grants no. PEst-C/EQB/LA0006/2013 and FCOMP-01-0124-FEDER-037285 and through projects ref. PTDC/CTM/108820/2008 and PTDC/CTM-POL/0813/2012 in the framework of Program COMPETE. The authors also acknowledge Operation NORTE-07-0124-FEDER-000067 – NANOCHEMISTRY. T.P. (SFRH/BD/89076/2012) and D.F. (SFRH/BPD/74877/2010) thank FCT for their grants.

REFERENCES

1. M.-S. Wang, G. Xu, Z.-J. Zhang and G.-C. Guo, *Chem. Commun.*, 2010, **46**, 361–376.
2. A. F. Little and R. M. Christie, *Color. Technol.*, 2010, **126**, 157–163.
3. M. Aldib and R. M. Christie, *Color Technol*, 2013, **129**, 131–143.
4. R. Pardo, M. Zayat and D. Levy, *Chem Soc Rev*, 2011, **40**, 672–687.
5. T. He and J. Yao, *Prog. Mater. Sci.*, 2006, **51**, 810–879.
6. T. Yamase, *Chem. Rev.*, 1998, **98**, 307–326.
7. A. Dolbecq, E. Dumas, C. R. Mayer and P. Mialane, *Chem. Rev.*, 2010, **110**, 6009–6048.
8. D. M. Fernandes, L. Cunha-Silva, R. A. S. Ferreira, S. S. Balula, L. D. Carlos, B. de Castro and C. Freire, *RSC Adv.*, 2013, **3**, 16697–16707.
9. M. Ammam, *J Mater Chem A*, 2013, **1**, 6291–6312.
10. J.-D. Compain, P. Deniard, R. Dessapt, A. Dolbecq, O. Oms, F. Sécheresse, J. Marrot and P. Mialane, *Chem. Commun.*, 2010, **46**, 7733–7735.
11. R. Dessapt, M. Collet, V. Coué, M. Bujoli-doeuff, S. Jobic, C. Lee and M. Whangbo, *Inorg. Chem.*, 2009, **48**, 574–580.
12. K. Binnemans, *Chem. Rev.*, 2009, **109**, 4283–4374.
13. Y. Han, Y. Xiao, Z. Zhang, B. Liu, P. Zheng, S. He and W. Wang, *Macromolecules*, 2009, **42**, 6543–6548.
14. A. Proust, B. Matt, R. Villanneau, G. Guillemot, P. Gouzerh and G. Izzet, *Chem. Soc. Rev.*, 2012, **41**, 7605–7622.
15. Y. Piao, A. Burns, J. Kim, U. Wiesner and T. Hyeon, *Adv. Funct. Mater.*, 2008, **18**, 3745–3758.
16. Y. Wang, A. D. Price and F. Caruso, *J. Mater. Chem.*, 2009, **19**, 6451–6464.
17. X. Luo and C. Yang, *Phys. Chem. Chem. Phys.*, 2011, **13**, 7892–7902.
18. W. Qi, H. Li and L. Wu, *J. Phys. Chem. B*, 2008, **112**, 8257–8263.
19. P. C. R. Soares-Santos, H. I. S. Nogueira, V. Fe, M. G. B. Drew, R. A. Sa, D. Carlos and T. Trindade, *Chem. Mater.*, 2003, **15**, 100–108.
20. M. Green, J. Harries, G. Wakefield and R. Taylor, *J. Am. Chem. Soc.*, 2005, **127**, 12812–12813.
21. K. O. Iwu, P. C. R. Soares-Santos, H. I. S. Nogueira, D. Carlos and T. Trindade, *J. Phys. Chem. C*, 2009, **5**, 7567–7573.
22. C. M. Granadeiro, R. A. S. Ferreira, P. C. R. Soares-Santos, L. D. Carlos, T. Trindade and H. I. S. Nogueira, *J. Mater. Chem.*, 2010, **20**, 3313–3318.

23. C. S. Neves, C. M. Granadeiro, L. Cunha-Silva, D. Ananias, S. Gago, G. Feio, P. A. Carvalho, P. Eaton, S. S. Balula and E. Pereira, *Eur. J. Inorg. Chem.*, 2013, **2013**, 2877–2886.

24. A. J. Gaunt, I. May, M. J. Sarsfield, D. Collison and I. S. Denniss, *Dalt. Trans.*, 2003, 2767–2771.

25. J. Kobler, K. Möller and T. Bein, *ACS Nano*, 2008, **2**, 791–799.

26. C. Pereira, C. Alves, A. Monteiro, C. Magén, A. M. Pereira, A. Ibarra, M. R. Ibarra, P. B. Tavares, J. P. Araújo, G. Blanco, J. M. Pintado, A. P. Carvalho, J. Pires, M. F. R. Pereira and C. Freire, *ACS Appl. Mater. Interfaces*, 2011, **3**, 2289–2299.

27. L. S. Ribeiro, T. Pinto, A. Monteiro, O. S. G. P. Soares, C. Pereira, C. Freire and M. F. R. Pereira, *J Mater Sci*, 2013, **48**, 5085–5092.

28. F. Rouquerol, J. Rouquerol, and K. Sing, *Adsorption by Powders and Porous Solids*, Academic Press, San Diego, 1999.

29. R. Al-Oweini and H. El-Rassy, *J. Mol. Struct.*, 2009, **919**, 140–145.

30. F. Breu, S. Guggenbichler, and J. Wollmann, *Structure Determination of Organic Compounds - Tables of Spectral Data*, Springer-Verlag, Berlin, Germany, 4th ed., 2009.

31. B. Lee, L. Bao, H. Im, S. Dai, E. W. Hagaman and J. S. Lin, *Langmuir*, 2003, **11**, 4246–4252.

32. R. Copping, A. J. Gaunt, I. May, M. J. Sarsfield, D. Collison, M. Helliwell, I. S. Denniss and D. C. Apperley, *Dalt. Trans.*, 2005, 1256–1262.

33. L. A. Combs-walker and C. L. Hill, *Inorg. Chem.*, 1991, **30**, 4016–4026.

34. L. Dermeche, R. Thouvenot, S. Hocine and C. Rabia, *Inorganica Chim. Acta*, 2009, **362**, 3896–3900.

35. X. Zhang, W. Wu, J. Wang, C. Liu and S. Qian, *J. Mater. Res.*, 2011, **23**, 18–26.

36. L. Bi, E. Wang, L. Xu and R. Huang, *Inorganica Chim. Acta*, 2000, **305**, 163–171.

37. T. R Zhang, W. Feng, R. Lu, C. Y Bao, T. Jin Li, Y. Ying Zhao and J. Nian Yao, *J. Solid State Chem.*, 2002, **166**, 259–263.

38. X. Zhang, W. Wu, Y. Man, T. Tian, X. Tian and J. Wang, *Sci. China Ser. B.*, 2007, **50**, 318–326.

39. J. Chen, L. Mei Ai, W. Feng, D. Q. Xiong, Y. Liu and W. M. Cai, *Mater. Lett.*, 2007, **61**, 5247–5249.

40. L.-M. Ai, W. Feng, J. Chen, Y. Liu and W. Cai, *Mater Chem Phys*, 2008, **109**, 131–136.

41. J. Iijima and H. Naruke, *Inorganica Chim. Acta*, 2011, **379**, 95–99.

42. M. Widodo, A. El-Shafei and P. J. Hauser, *J Polym Sci Pol Phys*, 2012, **50**, 1165–1172.

43. E. Poverenov, M. Shemesh, A. Gulino, D. A. Cristaldi, V. Zakin, T. Yefremov and R. Granit, *Colloid Surf. B*, 2013, **112**, 356–361.

44. M. M. Chehimi, *J Catal*, 2002, **196**, 187–196.

45. D. M. Fernandes, J. G. Vos and C. Freire, *J Colloid Interf Sci*, 2014, **420**, 127–135.

46. J. F. Moulder, W. F. Stickle, P. E. Sobol and K. D. Bomben, *Handbook of X-ray Photoelectron Spectroscopy*, Physical Electronics, Eden Prairie, MN, 1995.

47. Z. J. Ku, Z. H. Zhang, K. L. Zhang and Y. Ding, *Russ. J. Coord. Chem.*, 2008, **34**, 454–460.

48. D. M. Fernandes and C. Freire, *J Appl Electrochem*, 2014, **44**, 655–665.

49. Z. Wang, R. Zhang, Y. Ma, L. Zheng, A. Peng, H. Fu and J. Yao, *J. Mater. Chem.*, 2010, **20**, 1107–1111.

50. P. V. Bernhardt, B. M. Flanagan, M. J. Riley and B. J. Wood, *J Electron Spectrosc*, 2002, **124**, 73–77.

51. P. Tian, J. Cheng and G. Zhang, *Appl. Surf. Sci.*, 2011, **257**, 4896–4900.

52. D. M. Fernandes, D. Julião, C. Pereira, D. Ananias, S. S. Balula and C. Freire, *Colloids Surfaces A Physicochem. Eng. Asp.*, 2012, **415**, 302–309.

53. J. Zhao, D. Shi, L. Chen, Y. Li, P. Ma, J. Wang and J. Niu, *Dalt. Trans.*, 2012, **41**, 10740–10751.

CAPTIONS TO FIGURES

Fig. 1 FTIR-ATR spectra of (A) C18, (B) C18-SiO_2, (C) C18-SiO_2@$Tb(PMo_{11})_2$ and (D) $Tb(PMo_{11})_2$ in the (a) 4000–650 cm^{-1} and (b) magnified 2000–650 cm^{-1} regions. Dashed rectangle: characteristic vibrational bands of the lanthano phosphomolybdate.

Fig. 2 Raman spectra of (A) C18-SiO_2, (B) C18-SiO_2@$Tb(PMo_{11})_2$ and (C) $Tb(PMo_{11})_2$ in the 1100–400 cm^{-1} range. Dashed rectangle: characteristic vibrational bands of the lanthano phosphomolybdate.

Fig. 3 Deconvoluted XPS high-resolution spectra of C18-SiO_2@$Tb(PMo_{11})_2$ in the O 1s, Mo 3p, N 1s, Mo 3d and Tb 3d core-level regions. The overall simulated spectra are represented by brown lines.

Fig. 4 SEM micrographs of (A) C18-SiO_2, (B) C18-SiO_2@PMo_{11} and (C) C18-SiO_2@$Tb(PMo_{11})_2$ -based nanomaterials. Inset of A–C: EDS spectra.

Fig. 5 N_2 adsorption-desorption isotherms at –196 ºC of (A) C18-SiO_2 and (B) C18-SiO_2@$Tb(PMo_{11})_2$.

Fig. 6 Diffuse reflectance spectra of C18-SiO_2@PMo_{11}, C18-SiO_2@$Sm(PMo_{11})_2$, C18-SiO_2@$Eu(PMo_{11})_2$, C18-SiO_2@$Gd(PMo_{11})_2$, C18-SiO_2@$Tb(PMo_{11})_2$ and C18-SiO_2@$Dy(PMo_{11})_2$ (a) before and (b) after UV irradiation at room temperature.

Fig. 7 Graph of CIELAB color values (a*, b*) of non-irradiated PMo_{11} and $Ln(PMo_{11})_2$-based hybrid nanomaterials (for simplification the $Ln(PMo_{11})_2$-based hybrid nanomaterials are denoted by the symbol of the lanthanide).

Fig. 8 Graph of CIELAB color values (a*, b*) of UV irradiated PMo_{11} and $Ln(PMo_{11})_2$-based hybrid nanomaterials (for simplification the $Ln(PMo_{11})_2$-based hybrid nanomaterials are denoted by the symbol of the lanthanide).

Fig. 1

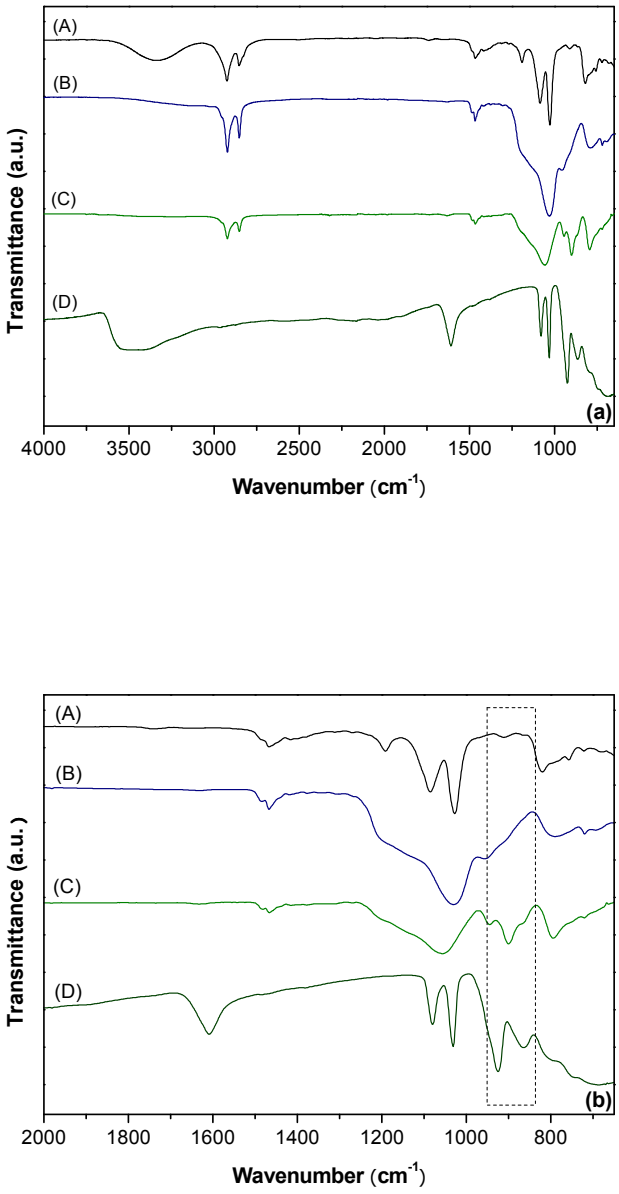

Fig. 2

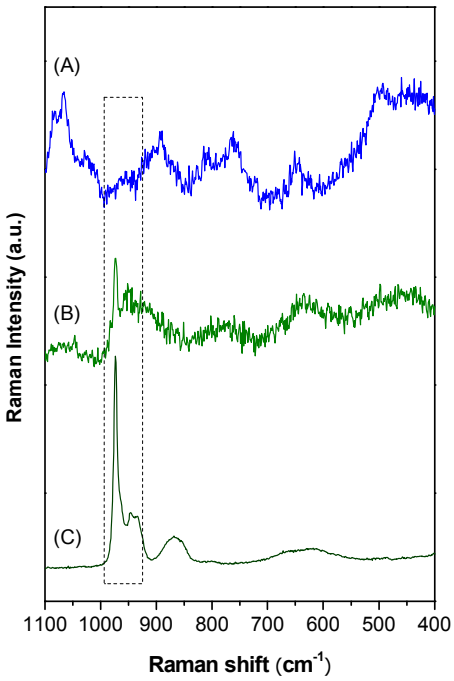

Fig. 3

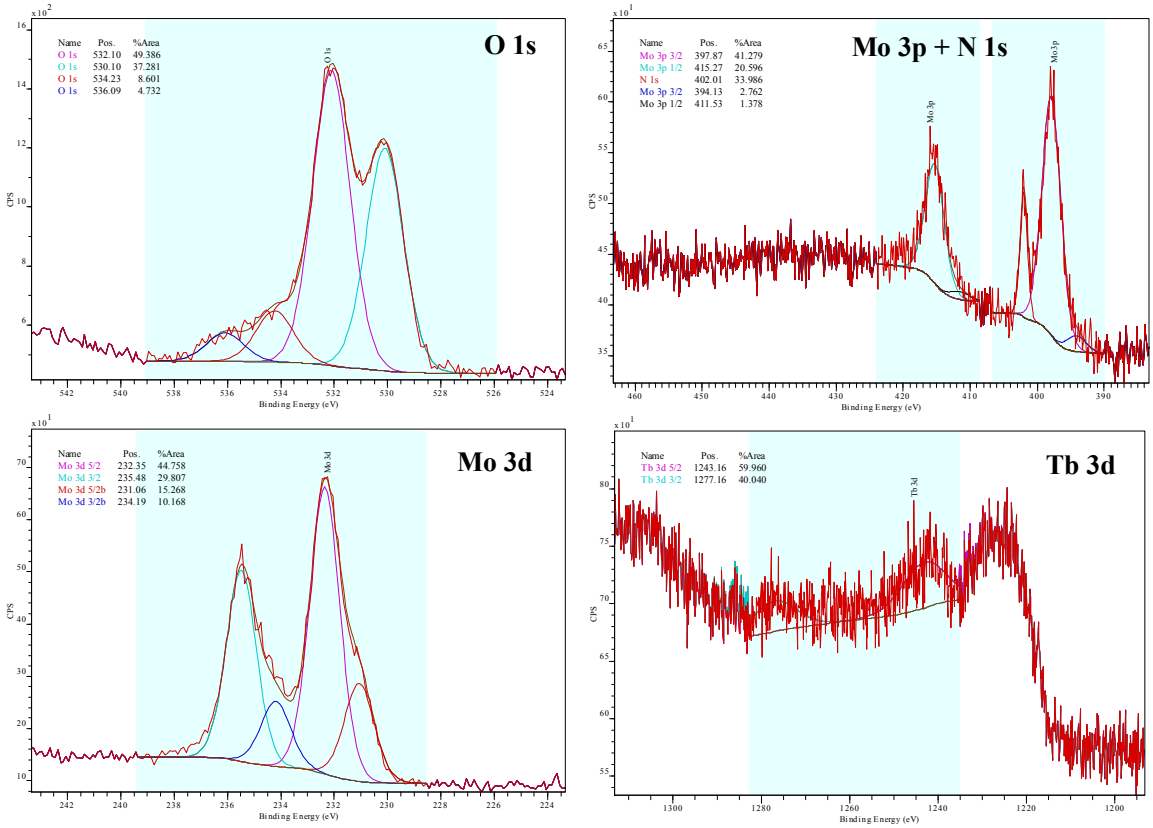

Fig. 4

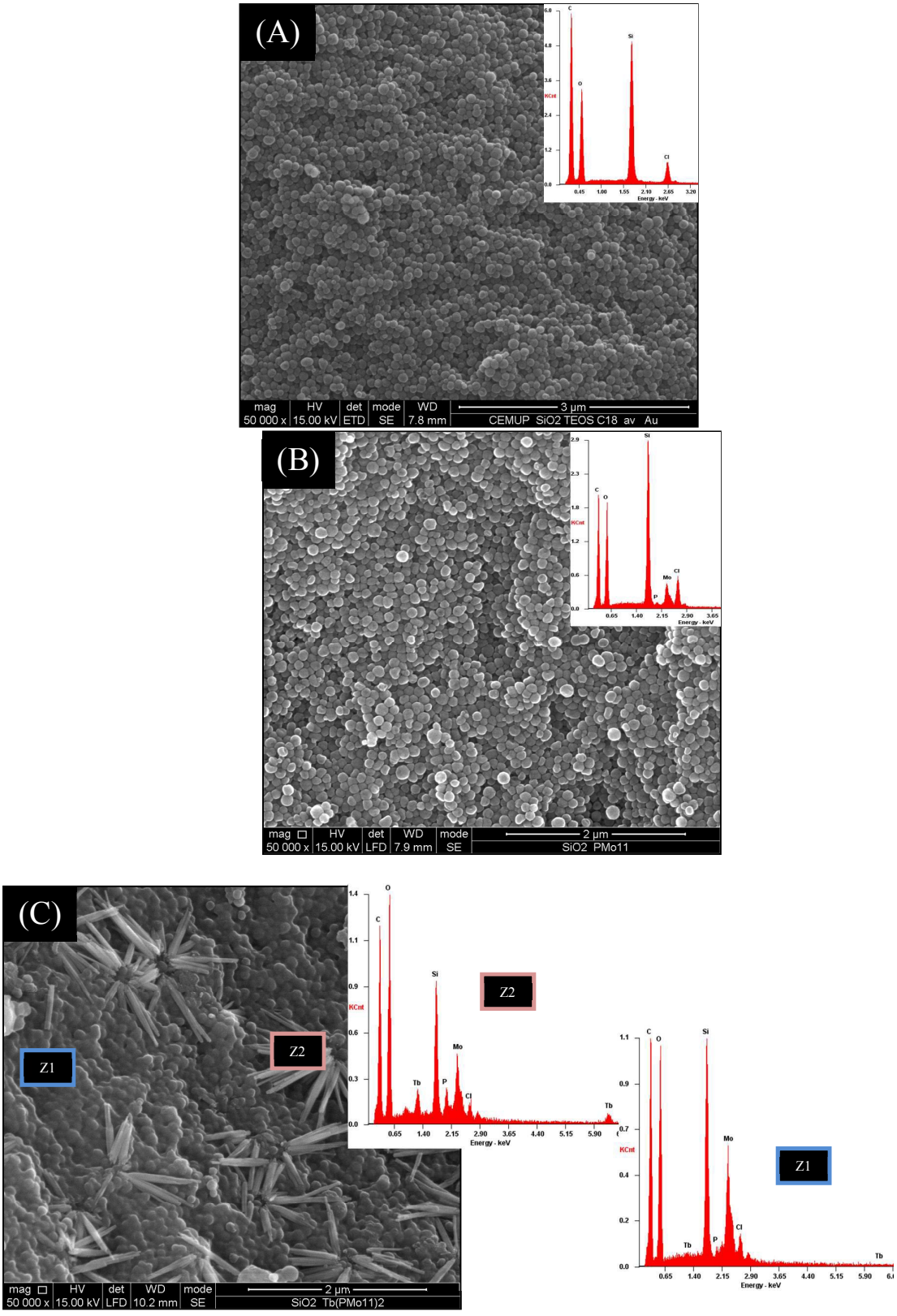

Fig. 5

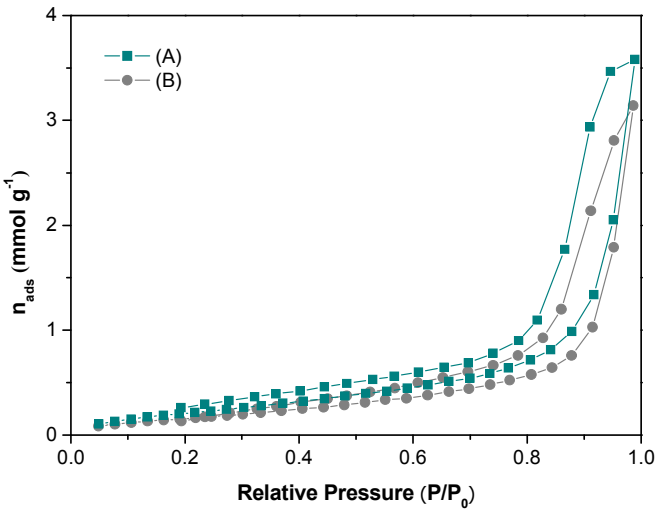

Fig. 6

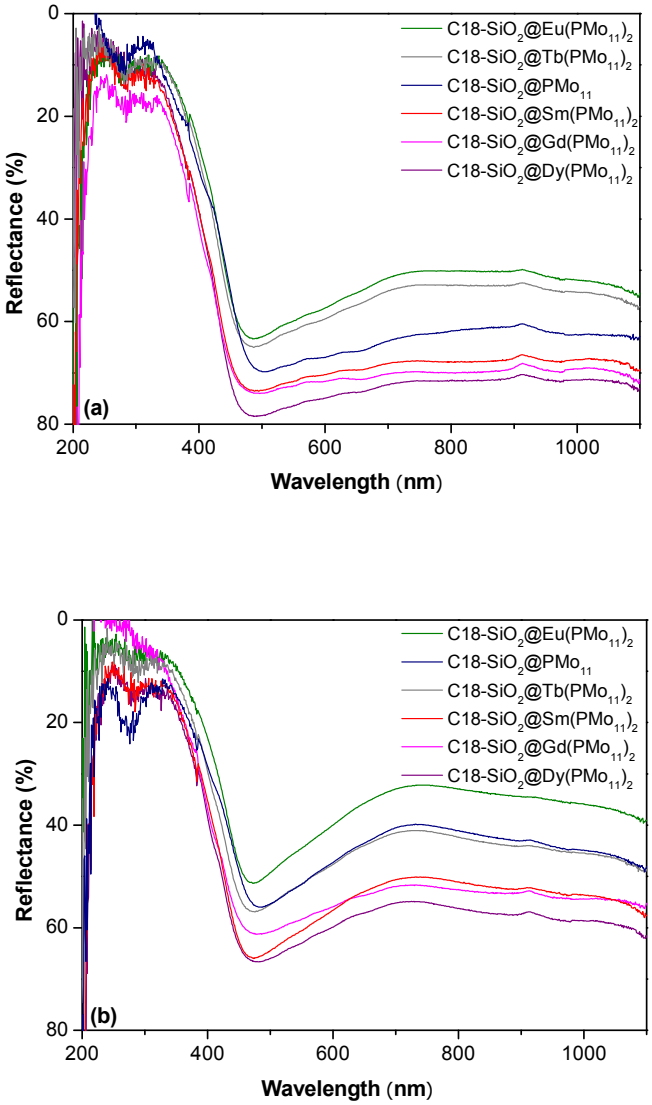

Fig. 7

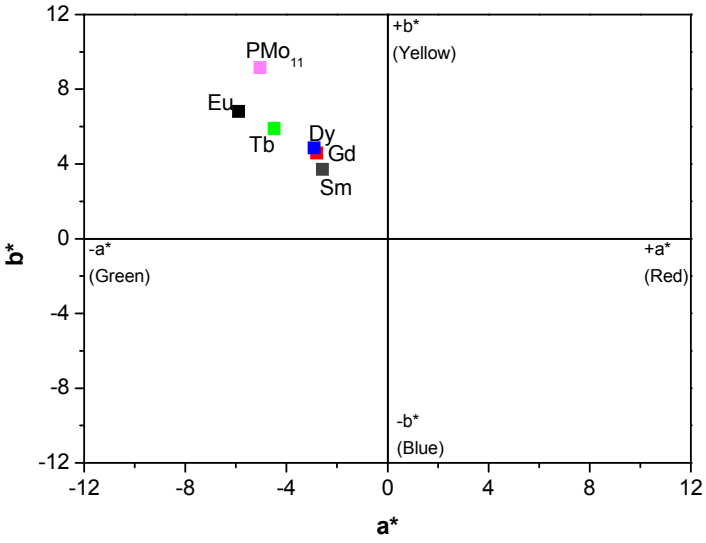

Fig. 8

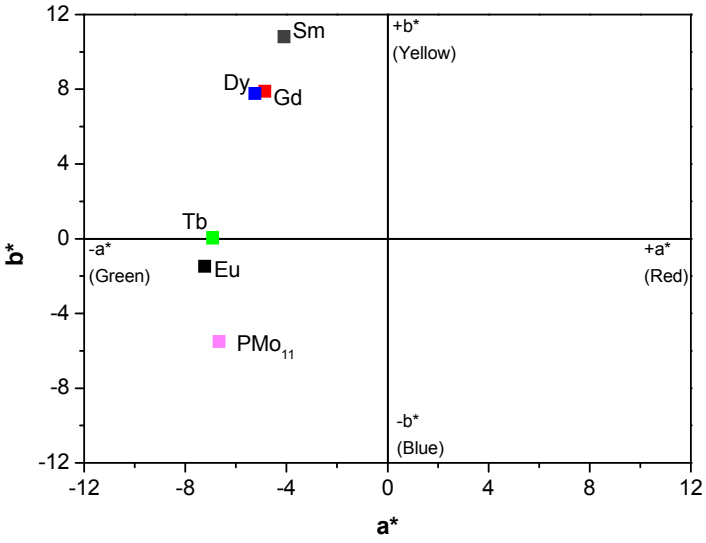

Table 1 Carbon, silicon, nitrogen and molybdenum contents of the silica-based hybrid nanomaterials determined by EA and ICP-AES

Material	Si (mmol g^{-1})	C (mmol g^{-1})	N (mmol g^{-1})	Mo (mmol g^{-1})
C18-SiO_2	7.0	32.8	1.4	
C18-SiO_2@PMo_{11}	6.6	29.1	1.1	0.8
C18-SiO_2@$Sm(PMo_{11})_2$	5.6	30.5	1.2	1.4
C18-SiO_2@$Eu(PMo_{11})_2$	4.9	28.4	1.1	1.7
C18-SiO_2@$Gd(PMo_{11})_2$	4.9	31.0	1.2	1.3
C18-SiO_2@$Tb(PMo_{11})_2$	5.0	28.9	1.1	1.7
C18-SiO_2@$Dy(PMo_{11})_2$	4.9	31.4	1.3	1.4

Table 2 Carbon, silicon, nitrogen and molybdenum surface atomic percentages of the silica-based nanomaterials obtained by XPS[a]

Material	Atomic %						
	C 1s	N 1s	O 1s	Si 2p	P 2p	Mo 3d	Ln 3d/4d
C18-SiO_2	66.3	1.8	21.6	10.2			
C18-SiO_2@PMo_{11}	65.4	1.6	24.5	7.7		0.8	
C18-SiO_2@$Sm(PMo_{11})_2$	71.7	2.4	18.5	4.1	0.8	2.1	0.4[c]
C18-SiO_2@$Eu(PMo_{11})_2$	66.6	2.2	22.6	5.2	0.1	3.1	0.2[d]
C18-SiO_2@$Gd(PMo_{11})_2$	66.8	2.0	22.0	6.6	0.3	1.7	0.6[e]
C18-SiO_2@$Tb(PMo_{11})_2$	66.2	1.8	23.4	5.2	0.4	2.7	0.3[f]
C18-SiO_2@$Dy(PMo_{11})_2$[b]	68.2	1.8	21.7	6.2	0.4	1.7	[b]

[a] Determined by the areas of the respective bands in the high-resolution XPS spectra. [b] Surface atomic percentages estimated without considering the Dy 3d surface content, which could not be determined since the Dy 3d relative sensitivity factor (RSF) is not reported in the literature or XPS libraries. [c] Surface atomic percentage estimated by curve fitting of the Sm 3d high-resolution spectrum. [d] Surface atomic percentage estimated through the Eu 4d band. [e] Surface atomic percentage estimated by curve fitting of the Gd 3d high-resolution spectrum, considering only the Gd $3d_{5/2}$ component since the Gd $3d_{3/2}$ component is overlapped with the carbon KLL Auger lines. [f] Surface atomic percentage estimated through the Tb 4d band due to the lack of published Tb 3d RSF.

Table 3 Textural properties of the silica-based hybrid nanomaterials

Material	A_{BET}[a] (m^2 g^{-1})	V_{pore}[b] (cm^3 g^{-1})	d_{pore}[c] (nm)
C18-SiO_2	20	0.12	13.65
C18-SiO_2@PMo_{11}	33	0.17	19.15
C18-SiO_2@$Sm(PMo_{11})_2$	17	0.09	3.42
C18-SiO_2@$Eu(PMo_{11})_2$	23	0.07	3.40
C18-SiO_2@$Gd(PMo_{11})_2$	19	0.08	3.42
C18-SiO_2@$Tb(PMo_{11})_2$	16	0.10	19.21
C18-SiO_2@$Dy(PMo_{11})_2$	18	0.08	3.41

[a] Specific surface area. [b] Total pore volume. [c] Pore diameter defined as the maximum on the pore size distribution which was determined by the BJH method from the desorption branch of the N_2 isotherm.

Table 4 CIELAB color values (L*, a*, b*) and color difference ΔE* between UV irradiated and non-UV irradiated silica-based hybrid nanomaterials

Material	non-UV irradiated			UV irradiated			ΔL*	Δa*	Δb*	ΔE*
	L*	a*	b*	L*	a*	b*				
C18-SiO_2@PMo_{11}	90.1	-5.0	9.2	67.7	-6.7	-5.5	-22.4	-1.6	-14.7	26.9
C18-SiO_2@Sm(PMo_{11})$_2$	92.0	-2.6	3.7	85.0	-4.1	10.8	-6.9	-1.5	7.1	10.0
C18-SiO_2@Eu(PMo_{11})$_2$	86.1	-5.9	6.8	69.1	-7.2	-1.5	-17.0	-1.3	-8.3	18.9
C18-SiO_2@Gd(PMo_{11})$_2$	92.0	-2.8	4.6	81.9	-4.9	7.9	-10.1	-2.1	3.3	10.8
C18-SiO_2@Tb(PMo_{11})$_2$	88.7	-4.5	5.9	71.0	-6.9	0.0	-17.7	-2.4	-5.9	18.8
C18-SiO_2@Dy(PMo_{11})$_2$	92.1	-2.9	4.9	80.9	-5.2	7.8	-11.2	-2.3	2.9	11.8

Graphical Abstract

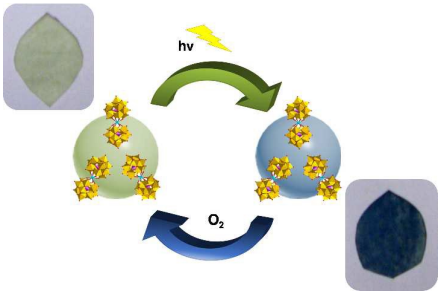

Novel hybrid nanomaterials prepared through the immobilization of the lacunary Keggin-type phosphomolybdate (PMo_{11}) and sandwich-type lanthano phosphomolybdates $Ln(PMo_{11})2$, (Ln^{III} = Sm, Eu, Gd, Tb and Dy) onto positively-charged functionalized silica nanoparticles revealed promising photochromic properties under UV irradiation (λ = 254 nm)